Showcasing research from Professor Baolong Shen's laboratory, Southeast University, Nanjing, China.

Vacancy induced microstrain in high-entropy alloy film for sustainable hydrogen production under universal pH conditions

We propose a novel strain-engineering approach to improve the electrocatalytic efficiency of high-entropy alloy (HEA) by introducing vacancy-induced microstrain into the HEA films. The engineered HEA film exhibits economically feasible industrial water electrolysis capabilities under pH universal conditions, achieving overpotentials of 104 mV (alkaline) and 106 mV (acidic) at 1 A cm^{-2}. Multi-element active sites with low coordination environments enhance charge transferability, thereby improving water adsorption and dissociation capacity. Additionally, the microstrain effect shifts the d-band center of Pt to an optimal position, enhancing hydrogen evolution reaction activity.

ROYAL SOCIETY OF **CHEMISTRY**

rsc.li/ees

Check for updates

Vacancy induced microstrain in high-entropy alloy film for sustainable hydrogen production under universal pH conditions†

Yiyuan Yang,[a] Zhe Jia, [iD] *[a] Qianqian Wang,[a] Yujing Liu,[b] Ligang Sun,*[c] Bo Sun,[a] Juan Kuang,[a] Shoujun Dai,[d] Jianguo He,[d] Sida Liu,[e] Lunbo Duan, [iD] [f] Hongjian Tang,[f] Lai-Chang Zhang,[g] Jamie J. Kruzic [iD] [h] Jian Lu [iD] [i] and Baolong Shen [iD] *[a]

Electrocatalytic hydrogen production plays an essential role in generating eco-friendly fuels for energy storage and transportation within a sustainable energy framework. High-entropy alloys (HEAs), with their abundant compositional variety, significantly expand the scope of material libraries and have received substantial research interest in energy and environmental technologies. However, the conventional approach to modulating HEA catalysts through element selection and exploiting the cocktail effect overlooks the potential of the high designability of high-entropy solid solutions. Herein, we present a novel strain engineering strategy to further enhance the catalytic performance of a desirable HEA composition by incorporating vacancy-induced microstrain into an HEA film. The strain engineered HEA film delivers an economically viable industrial water electrolysis capacity at an ampere-level current density of 1 A cm^{-2} with overpotentials of 104 and 106 mV under alkaline and acidic conditions, respectively. Remarkably, it retains long-term sustainability of $\sim$500 h at 100 mA cm^{-2} in an anion exchange membrane (AEM) device, demonstrating a lifespan 40 times that of a commercial Pt/C||IrO$_2$ system. Microstructural analyses and computational calculations indicate that the active sites with a low coordination environment enhance charge transferability, and thus promote the water adsorption capacity. Furthermore, the microstrain effect downshifts in the d-band center of Pt to a near-optimal position, which subsequently lowers the binding affinity between Pt and intermediates, resulting in enhanced hydrogen evolution reaction activity. Our work demonstrates a practical strain engineering strategy that provides a new avenue to enhance the performance of catalysts for sustainable energy conversion.

Broader context

Electrical water splitting is a promising avenue for producing green hydrogen, crucial for achieving future carbon neutrality goals. High-entropy alloys (HEAs) have attracted considerable interest in energy conversion, yet precise atomic-level structural design remains a formidable challenge. Here, we propose a novel strain engineering approach to improve the catalytic efficiency of HEA compositions by introducing vacancy-modulated microstrain into an HEA film. The engineered HEA film exhibits economically feasible industrial water electrolysis capabilities under pH universal conditions, achieving an ampere-level current density of 1 A cm^{-2} with overpotentials of 104 and 106 mV under alkaline and acidic conditions, respectively. Impressively, it maintains long-term sustainability for approximately 500 hours at 100 mA cm^{-2} in an anion exchange membrane (AEM) device, the lifespan of which is 40 times as long as the commercial noble-metal system Pt/C||IrO$_2$. Microstructural analyses and computational simulations suggest that multi-element active sites with low coordination environments enhance charge transferability, thereby improving water adsorption and dissociation capacity. Additionally, the microstrain effect shifts the d-band center of Pt to an optimal position, reducing the binding affinity between Pt and intermediates and enhancing hydrogen evolution reaction activity. This study not only provides a practical pathway for large-scale hydrogen production under pH universal conditions, but also highlights the effectiveness of nanoscale heterogeneous strain field in multi-principal catalysts for understanding and designing high-performance materials for sustainable energy conversion.

[a] School of Materials Science and Engineering, Jiangsu Key Laboratory for Advanced Metallic Materials, Southeast University, Nanjing, 211189, China. E-mail: zhejia@seu.edu.cn, blshen@seu.edu.cn

[b] Institute of Metals, College of Materials Science and Engineering, Changsha University of Science & Technology, Changsha, 410114, China

[c] School of Science, Harbin Institute of Technology, Shenzhen, 518055, China. E-mail: sunligang@hit.edu.cn

[d] Key Laboratory of Computational Optical Imaging Technology, Aerospace Information Research Institute, Chinese Academy of Sciences, Beijing, 100094, China

[e] Laboratory for Multiscale Mechanics and Medical Science, SV LAB, School of Aerospace Xi'an Jiaotong University, Xi'an, 710049, China

[f] Key Laboratory of Energy Thermal Conversion and Control, Ministry of Education, School of Energy and Environment, Southeast University, Nanjing, 210096, China

[g] Centre for Advanced Materials and Manufacturing, School of Engineering, Edith Cowan University, 270 Joondalup Drive, Joondalup, Perth, WA 6027, Australia

[h] School of Mechanical and Manufacturing Engineering, University of New South Wales (UNSW Sydney), Sydney, NSW 2052, Australia

[i] Hong Kong Branch of National Precious Metals Material Engineering Research Center and Department of Mechanical Engineering, City University of Hong Kong, Hong Kong SAR, China

† Electronic supplementary information (ESI) available. See DOI: https://doi.org/10.1039/d4ee01139b

5854 | *Energy Environ. Sci.,* 2024, **17**, 5854–5865

This journal is © The Royal Society of Chemistry 2024

Introduction

The production of clean hydrogen is a critical component of a sustainable energy future.[1,2] Renewable energy-driven water electrolysis presents a promising solution for green hydrogen production, given its high purity and environmentally friendly attributes.[3] However, an ongoing challenge lies in identifying cost-effective and sustainable electrocatalysts that satisfy the requirements of industrial applications.[4–6] Highly active catalysts, such as single-atom materials,[7,8] layered double hydroxides,[9,10] MXenes,[11] and transition metal compounds,[12–15] have recently attracted attention for their adoption in the electrochemical hydrogen evolution reaction (HER).[16] Although they have extraordinary catalytic activity and selectivity, they fall short of industrial and sustainability requirements owing to their unsatisfactory long-term durability due to weak structural and catalytic stability.[5] This deficiency has prompted efforts to investigate new catalysts and establish design guidelines for their activation and stabilization.

High-entropy alloys (HEAs), also referred to as multi-principal element alloys, are emerging as potential candidates for water electrolysis.[17–21] The complex chemistry of these alloys offers a wide range of significant synergistic effects and tunable electronic structures that can overcome the constraints of adsorption-energy regulation.[22–25] Inspired by such advances, the introduction of the high entropy concept has injected a fresh vibrancy into the development of novel catalysts, e.g., high-entropy oxides,[26] high-entropy sulfides,[27] high-entropy intermetallics,[22,28] high-entropy metallic glasses,[29,30] and a recently reported high-entropy electrolyte.[31,32] Nonetheless, the potential for using high-entropy materials as catalysts is still a relatively new field that is far from being fully exploited. So far, the primary focus has been on selecting elements that provide synergetic interactions to enhance the catalytic performance, an approach that is commonly referred to as the high entropy cocktail effect.[33–36] In contrast, other fundamental and universal strategies for regulating the electronic configuration and modifying the catalytic behavior of HEAs, for example the strain engineering, have rarely been reported, which represents an underexplored avenue for further advancement in this field.

Strain engineering has increasingly gained attention for its effectiveness in altering the surface electronic structure of electrocatalysts and thus improving catalytic activity.[37–41] Lattice strain, also known as microstrain,[42] is a measure used to quantify how much atoms deviate from their ideal positions within a crystal structure. It is typically generated by adopting various engineering strategies, including the use of solid solution alloys,[43] mismatches in lattice constants,[44,45] and the presence of structural defects such as vacancies,[42,46] twin boundaries,[47] and grain boundaries.[48–50] Both compressive and tensile strains have the ability to alter the position of the d-band center and adjust the binding energy of adsorbates.[51,52] This has been effectively illustrated in numerous electrocatalytic reactions including water splitting,[53,54] oxygen reduction reaction,[55–57] ethanol oxidation reaction,[58] formic acid oxidation reaction,[59] and carbon dioxide reduction reaction.[60,61] Nonetheless, the precise control of micros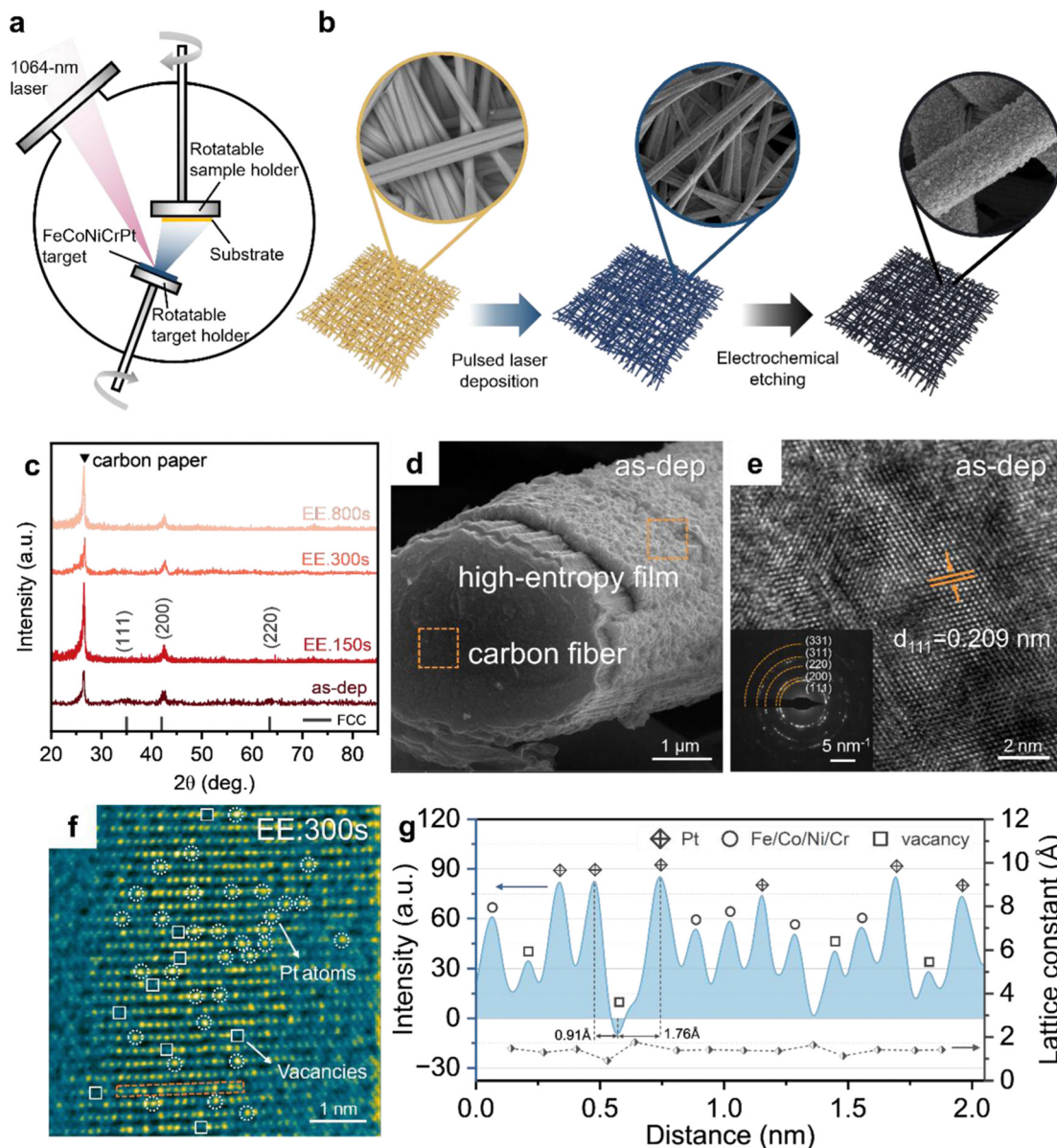train continues to present a significant challenge as the synthesis process usually requires strict regulation. In addition, the strain effect often coincides with the ligand effect,[62,63] which complicates the precise control of the strain intensity and the elucidation of the correlation between strain and activity. Furthermore, electrocatalysts driven by strain are typically thermodynamically metastable, leading to challenges concerning material stability.[47,64] Within this context, the concept of random solid solutions in HEAs offers a myriad of equally possible and theoretically infinite atomic coordination possibilities. This effectively mitigates the distracting ligand effect frequently encountered in traditional strain-related electrocatalysts.[63,65] Consequently, the integration of strain engineering and high-entropy concepts is expected to be a powerful approach for catalyst design, providing theoretical insights into this emerging high entropy catalytic material.

Herein, we present a study on a FeCoNiCrPt HEA film prepared via pulsed laser deposition (PLD) and subsequently treated electrochemically in an acid solution. The components are carefully chosen based on their intrinsic activity and electrode potential to ensure the electrochemical treatment selectively stripped away atoms from the surface, leading to abundant vacancies in lattice to generate a microstrain field. Particularly, the HEA that was acid treated for 300 seconds (denoted as EE.300s hereafter) exhibited robust strain fluctuations. The compressive strain was predominantly observed near the vacancies, whereas the tensile strain was primarily associated with Pt atoms. Benefiting from such vacancy-induced microstrain, the EE.300s HEA achieved overpotentials of 18, 46, and 73 mV at a current density of 10 mA cm^{-2} for HER under alkaline, acidic, and neutral conditions, respectively. Moreover, it only required overpotentials of 104 and 106 mV to drive the ampere-level current density of 1 A cm^{-2} under alkaline and acidic conditions respectively. The measured faradaic efficiency for H$_2$ production and the turnover frequency for the EE.300s HEA film were 99.1% at 500 mA cm^{-2} and 0.254 s^{-1} at an overpotential of 100 mV, respectively, surpassing most state-of-the-art electrocatalysts. Furthermore, we assembled the EE.300s HEA as the cathode in an anion exchange membrane (AEM) electrolyzer to investigate its potential for practical water electrolysis and its long term stability. It only required 2.0 V cell voltage to achieve a current density of 100 mA cm^{-2}, while maintaining stability for ~500 h with negligible activity degradation, performing 40 times longer than that of the commercial Pt/C catalyst. Theoretical analyses revealed that the microstrain distribution in EE.300s HEA film plays a crucial role in water molecule adsorption and water dissociation processes, and facilitates the shift of d-band center away from the Fermi level, thus weakening the overly strong interaction strength between H* and active sites.

Results and discussion

Preparation and characterization of the high-entropy film

The HEA film with an equal atomic composition of FeCoNiCrPt was prepared by the PLD technique (Video S1, ESI†). A schematic of the preparation process is presented in Fig. 1(a).

This journal is © The Royal Society of Chemistry 2024

Energy Environ. Sci., 2024, **17**, 5854–5865 | **5855**

Fig. 1 Preparation and characterization of FeCoNiCrPt HEA films. Schematic diagrams of the (a) PLD and (b) electrochemical etching processes of the HEA film on a carbon paper substrate. (c) GIXRD profile of the HEA films before and after electrochemical etching. (d) SEM image and (e) HRTEM image with SAED pattern (inset) of the as–dep HEA film. (f) HRTEM image of the EE.300s HEA film, where Pt atoms are marked by white dotted circles, and vacancies are marked by white squares. (g) Integrated pixel intensity profile for the EE.300s HEA film derived from the dotted orange box in (f), where peaks and valleys represent the atomic column and gap positions, respectively.

Carbon paper and commercial Ni foam were selected as the substrates for the PLD (Fig. S1, ESI†). The particulate-like surface (Fig. 1(d) and Fig. S2, ESI†), which contributes to the large specific exposed area of the electrode, is attributed to the fragmentation of the metastable melt caused by shock and rarefaction waves.[66] Grazing incidence X-ray diffraction (GIXRD) analysis indicated that the freshly deposited (denoted as as-dep) FeCoNiCrPt high-entropy film exhibited a face-centered cubic (FCC) structure (Fig. 1(c)), which was also confirmed by selected area election diffraction (SAED) and high-resolution transmission electron microscopy (HRTEM) (Fig. 1(e)), where a d-spacing of 0.209 nm was determined for the {111} plane. Moreover, inductively coupled

plasma-optical emission spectrometry (ICP-OES) measured different element ratios in the as-dep HEA film which are similar to the nominal composition we designed (Table S1, ESI†). And energy dispersive X-ray spectroscopy (EDS) elemental analysis further confirmed the homogeneous distributions of Fe, Co, Ni, Cr, and Pt elements (Fig. S3 and Table S1, ESI†).

To create a microstrain distribution on the film surfaces, the as-dep HEA films underwent post-treatment in 0.5 M H_2SO_4 solution to selectively remove the unstable surface atoms to induce lattice microstrain (Fig. 1(b)). Samples electrochemically etched for 150, 300, and 800 seconds were denoted as EE.150s, EE.300s, and EE.800s, respectively. The post-treatment retained

5856 | *Energy Environ. Sci.*, 2024, **17**, 5854–5865

This journal is © The Royal Society of Chemistry 2024

the rough surface morphology (Fig. S4, ESI†). GIXRD result indicated that the treated film retained the FCC structure (Fig. 1(c)), which was confirmed by the SAED pattern (Fig. S5, ESI†). As depicted in Fig. S6 and Table S1 (ESI†), the components retained homogeneous distributions. In particular, ICP-OES and EDS analyses both showed similar variation trend among four samples that the Pt content of EE.300s film was the highest, and relative decreases of Co and Ni was observed following acid solution treatment.

Fig. 1(f) shows abundant vacancies (marked as white squares) emerged in the EE.300s sample as a result of the Co and Ni depletion at the film surface. This magnification level readily allows for Z-contrast to distinguish Pt from the other atomic species based on it much larger atomic number. The brighter spots indicated by dotted circles were identified as Pt atoms, and the darker spots as Fe/Co/Ni/Cr atoms. Fig. 1(g) presents the integrated pixel intensities for the FCC lattice derived from orange dotted box in Fig. 1(f). Various atomic species as well as vacancies were classified according to discrepancies in intensity. The atomic distances, as calculated and depicted in Fig. 1(g) and Table S2 (ESI†), exhibited substantial fluctuations due to local

crystal cell volume expansions or contractions, particularly in areas adjacent to the vacancies. These distances ranged from a minimum of 0.91 Å to a maximum of 1.76 Å, signifying a substantial lattice strain in the acid-treated film.

We further analyzed the microstrain distribution for the HEA films before and after etching using geometric phase analysis (GPA), Fig. 2(a)–(c) shows that the normal strain (ε_{xx}) was negligible in most areas of the as-dep HEA film and was only concentrated at a few locations (bright red/blue spots), the value of which was in the range of -5% (compressive strain) to $+5\%$ (tensile strain). The strain concentration may be attributed to local lattice distortion or certain types of defects,[67–70] which is one of the four "core" effects of high-entropy alloy.[71] In the as-dep HEA film, different atom sizes of five principal components that make up crystal lattices of complex solid solution generated lattice distortion. And tiny distortion was gradually accumulated and finally produced local severe lattice distortion or misfit, which showed strain concentration in GPA. With respect to the EE.300s film, the introduction of large amount of vacancies resulted in displacement at surrounding lattice sites and caused microstrain fluctuation and inhomogeneity, as
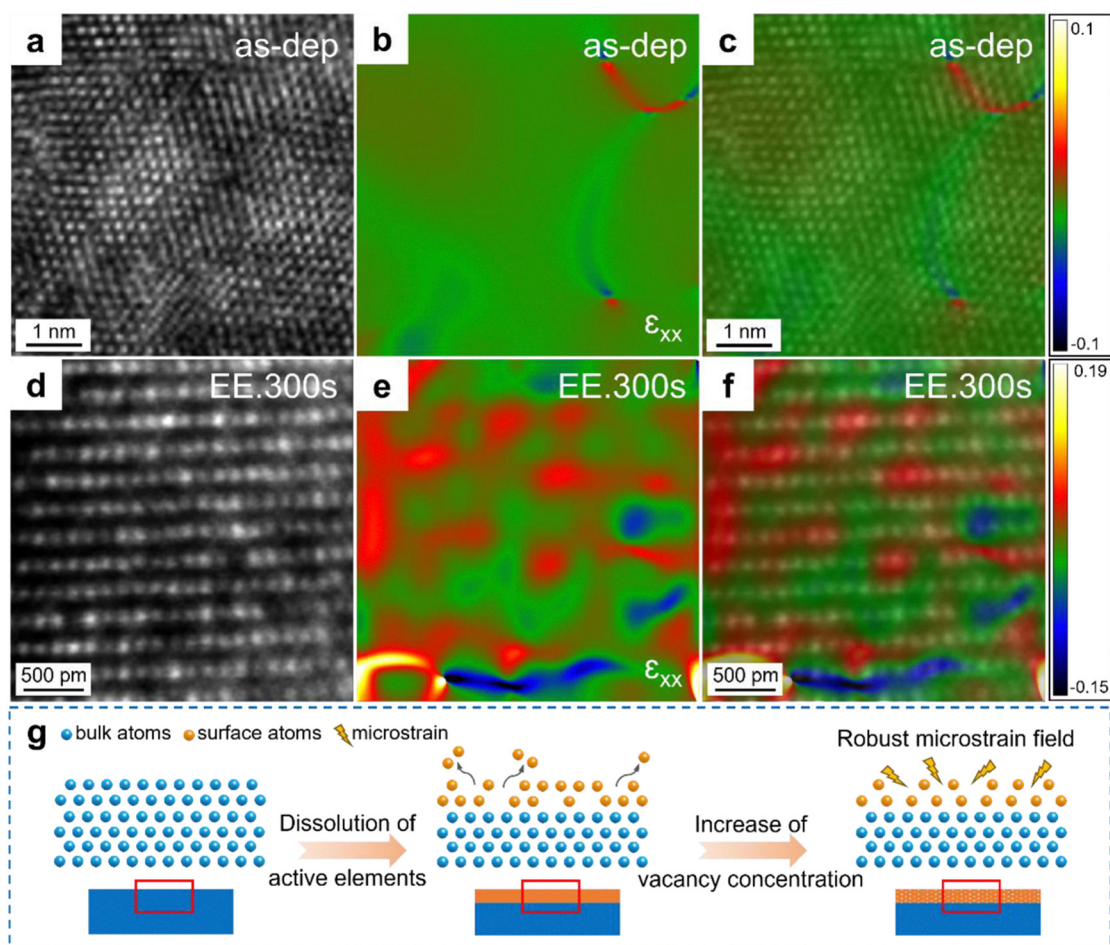

Fig. 2 Microstrain characterization of FeCoNiCrPt HEA films. (a) Lattice-resolution HRTEM image of the as–dep HEA film. (b) and (c) GPA images for normal strain (ε_{xx}) analysis of the as-dep HEA film. (d) Lattice-resolution HRTEM image of the EE.300s HEA film. (e) and (f) GPA images for ε_{xx} analysis of the EE.300s film. (g) Schematic illustration for the generation of microstrain in HEA film during the electrochemical treatment.

This journal is © The Royal Society of Chemistry 2024

Energy Environ. Sci., 2024, **17**, 5854–5865 | **5857**

confirmed by the GPA images (Fig. 2(d)–(f)). The ε_{xx} value was in the range of −15% to +19%, which was far greater than values for the as-dep, EE.150s, and EE.800s samples (Fig. S7, ESI†). Interestingly, the strain distribution was related to the vacancies and elemental distribution. As shown in Fig. 2(f), the regions with large tensile strain were enriched around the Pt atoms, while the compressive strain surrounded the regions of vacancies. When larger Pt atoms occupy lattice sites, the resulted lattice expansion will cause tensile strain on the lattice surrounding them. Conversely, the lattice will shrink when vacancies form during electrochemical treatment so that compressive strain generates

on the atoms near vacancies. On the basis of the experimental data, the origin of the microstrain in electrochemically etched HEA films is depicted in Fig. 2(g). The vacancies formed during the etching process serve as the sole source of the microstrain.

Analyses of electronic structure and atomic configuration

To gain insight into the atomic configuration of the HEA film surface, we adopted aberration-corrected TEM (AC-TEM) and high-resolution EDS mapping to assess the elemental distribution. The investigation revealed that elements Fe, Co, Ni, Cr, and Pt had a uniform distribution (Fig. 3(a)). Furthermore, no
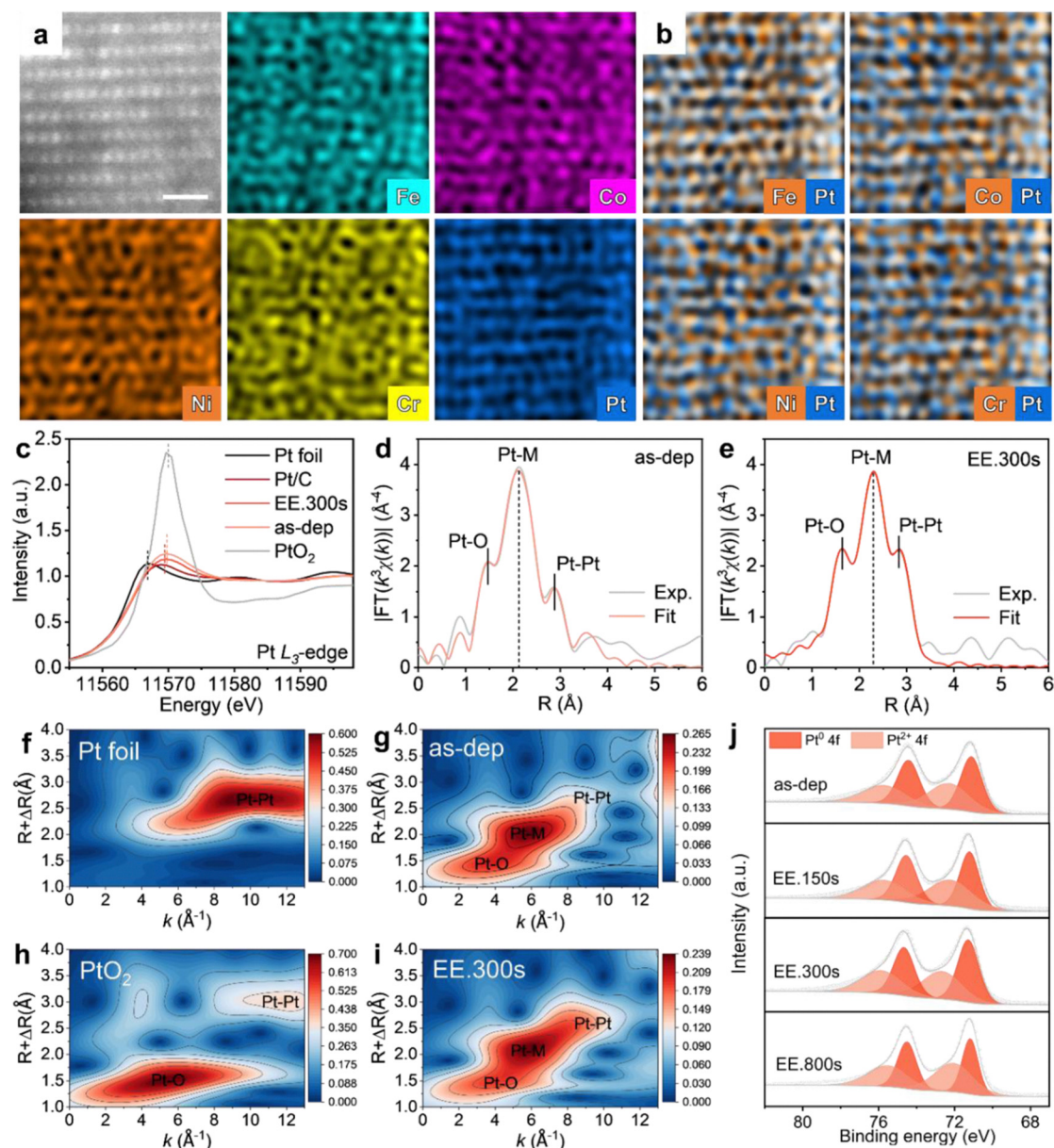
Fig. 3 Electronic structure and atomic configuration analyses of FeCoNiCrPt HEA films. (a) and (b) HAADF-STEM image and atomic-resolution EDS mapping of the EE.300s film, where the scale bar is 500 pm. (c) Pt L_3-edge XANES spectra for the Pt foil, Pt/C, PtO_2, as-dep, and EE.300s films. The Fourier transform of the k^3-weighted Pt L_3-edge EXAFS spectra for (d) as-dep, and (e) EE.300s HEA films, showing the strain effect on the Pt–M and Pt–Pt bond lengths. (f)–(i) Wavelet transform of the k^3-weighted Pt L_3-edge EXAFS results for Pt foil, as-dep, PtO_2, and EE.300s films, respectively. (j) Pt 4f XPS spectra for the as-dep, EE.150s, EE.300s, and EE.800s films.

sublattice occupation of any particular element was observed (Fig. 3(b)), implying that the EE.300s film was characterized by a chemically disordered solid solution. X-ray absorption near-edge spectroscopy (XANES) was carried out to monitor the bond lengths and Pt valence states on the surface of the HEA films for various microstrain statuses. Pt L_3-edge XANES was conducted to probe the average Pt valence state in the HEA films, in comparison with the spectra of Pt reference materials. As expected, the Pt L_3-edge white line intensities of the as-dep and EE.300s films were between those of Pt foil and PtO_2, and the peak position was clearly shift to the right relative to that for the Pt foil (Fig. 3(c)), indicating that the Pt atoms on the sample surface were coordinated with other metallic atoms, resulting in a Pt oxidation state. Fig. S8 and Table S3 (ESI†) indicated that the valence state of Pt decreases from 3.41 on the as-dep HEA film sample surface to 2.65 on the EE.300s sample surface. This decrease is attributed to an increased vacancy concentration after the electrochemical etching process.[72] The characterization results indicate that the etching process would lead to a microstrain effect due to the formation of vacancies. Furthermore, we conducted extended X-ray absorption fine structure (EXAFS) spectra and wavelet transformation analyses to reveal the atomic coordination structures of the as-dep and EE.300s HEA films (Fig. 3(d) and (e)). The detailed structural information is summarized in Table S4 (ESI†). The total coordination number of the as-dep HEA film, which was 7.1, was significantly lower than the value of 12 for the Pt foil. This number further reduced to 6.8 for the EE.300s HEA film, indicating that more dangling bonds existed on the EE.300s HEA film surface which would facilitate the adsorption of water molecules.[73] Moreover, it was found that the Pt–M bond length (M = Fe, Co, Ni, Cr) for the first shell in the EE.300s sample was 2.588 Å, which is slightly longer than for the as-dep HEA film (2.567 Å). Meanwhile, the Pt–Pt bond length in the EE.300s HEA film is 3.110 Å, which is shorter compared to the as-dep HEA film (3.147 Å). Such experimental phenomenon can be attributed to the lattice microstrain effect of the HEA film. The wavelet transform of the k^3-weighted Pt L_3-edge EXAFS results presented in Fig. 3(f)–(i) revealed that the Pt–M coordination ratio was the highest among all types of bonds for the as-dep and EE.300s HEA films, and the quantity of the Pt–Pt bonds increases after electrochemical treatment compared with the as-dep film. The EXAFS results further confirmed the presence of vacancy-induced microstrain in the EE.300s HEA film, which was in agreement with the HRTEM and GPA analyses.
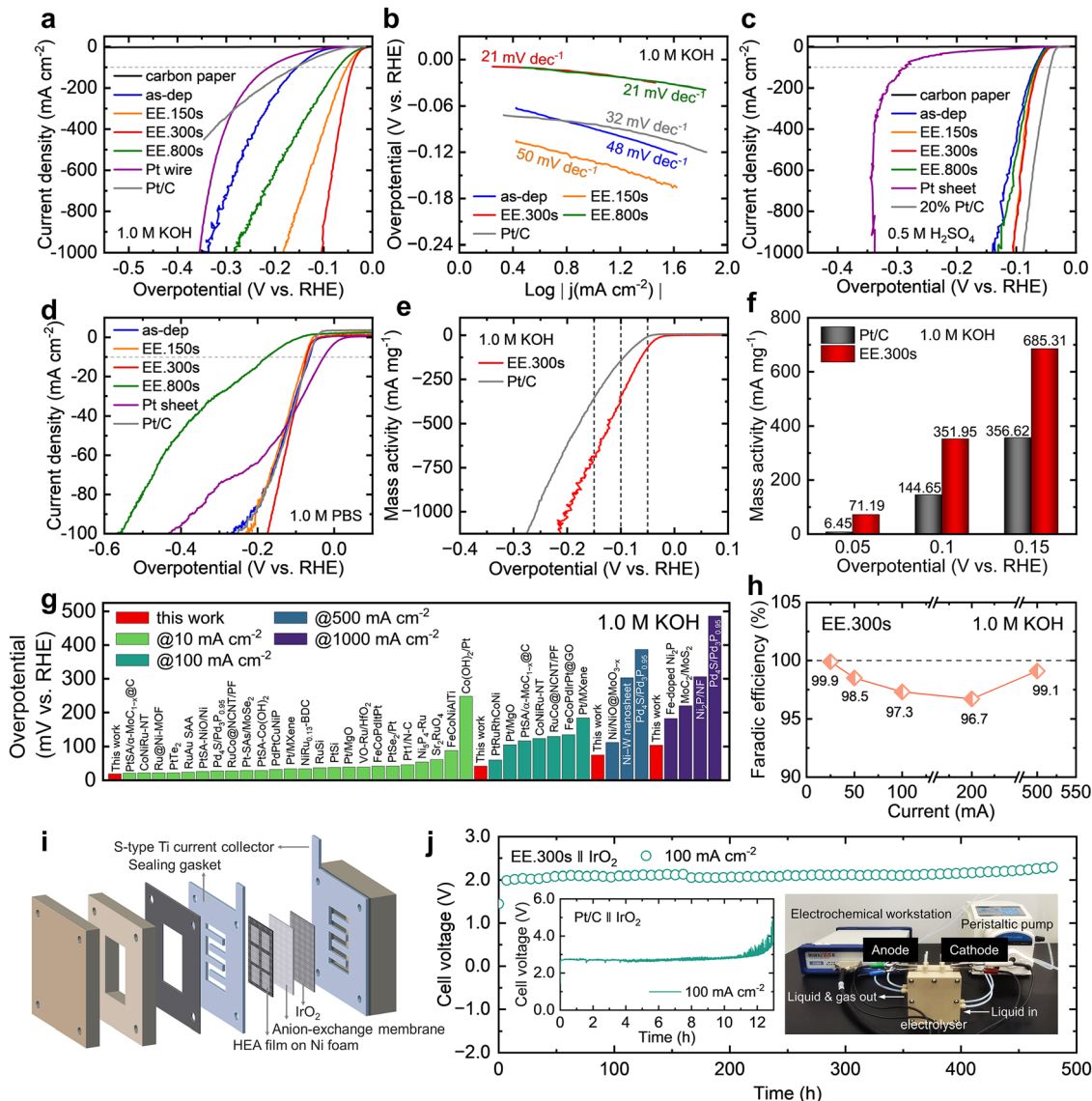
X-ray photoelectron spectroscopy (XPS) was also employed to investigate the electronic structures and chemical valence states of the HEA films (Fig. 3(j) and Fig. S9, ESI†). It was found that the EE.300s HEA film had Fe 2p peaks at 706.7 (Fe^0), 708.9 (Fe^{2+}), and 711.9 (Fe^{3+}) eV; Co 2p peaks at 777.8 (Co^0), 779.2 (Co^{3+}), and 781.0 (Co^{2+}) eV; Ni 2p peaks at 852.3 (Ni^0) and 854.7 (Ni^{2+}) eV; Cr 2p peaks at 574.4 (Cr^0) and 576.5 (Cr^{3+}) eV; Pt 4f peaks at 71.3 (Pt^0) and 72.7 (Pt^{2+}) eV; and O 1s peaks at 529.4 (M–O), 531.0 (M–OH), and 532.4 (adsorbed H_2O) eV, respectively. Compared with the chemical valence states of the as-dep HEA film, the EE.300s HEA sample had a larger quantity of

high-valent metallic elements. Moreover, it is noteworthy that the binding energies of Co 2p underwent positive shifts whereas Ni 2p and Cr 2p underwent negative shifts as the etching time increased, implying the loss and gain of electrons around the metal elements. Further extending the etching time to 800 seconds, the Ni 2p spectra presented a negative shift to the peak position close to EE.150s, which may be attributed to the over exposure of surface. The robust electron interaction among the elements suggests that the synergistic coexistence of multiple components amplified the local charge redistribution, potentially benefitting for the electrocatalytic activity. Furthermore, the abundant dangling bonds and lengthened Pt–M bonds in the EE.300s film suggest that the vacancy-induced microstrain improves the atomic coordination environment and the electronic structures of the HEA films, which would be beneficial to the HER activity.

Water electrolysis performance in pH-universal conditions

Water electrolysis activities of the as-dep and electrochemically etched samples were investigated under pH-universal environments. In 1.0 M KOH solution, the EE.300s HEA film with significant strain fluctuation exhibited an impressively low overpotential of 18 mV to achieve a current density of 10 mA cm^{-2} for HER (Fig. 4(a)). This was far superior to the as-dep HEA film (90 mV), EE.150s HEA film (19 mV), EE.800s HEA film (24 mV), and even Pt/C nanoparticles (62 mV) which are typically used as a benchmark for HER activity comparison. Moreover, the EE.300s sample demonstrated outstanding high-current-density activity, only 42 and 104 mV were required to drive current densities of 100 and 1000 mA cm^{-2}, respectively. This performance is among the highest in the representative state-of-the-art HER electrocatalysts (Fig. 4(g) and Table S5, ESI†). The EE.300s film also presented the smallest Tafel slope of 21 mV dec^{-1}, indicative of a Volmer–Heyrovsky reaction mechanism (Fig. 4(b)). Electrochemical impedance spectroscopy (EIS) results showed that the EE.300s HEA film manifests superior HER kinetics compared to its counterparts (Fig. S10, ESI†). Furthermore, our HEA film presented exceptional HER activity under the acidic and neutral conditions of 0.5 M H_2SO_4 and 1.0 M phosphate buffered saline (PBS) electrolytes. Under the acidic condition, the EE.300s HEA film displayed exceedingly low overpotentials of 46, 64, and 106 mV at current densities of 10, 100, and 1000 mA cm^{-2}, respectively (Fig. 4(c)), surpassing the performance of most currently reported electrocatalytic materials (Fig. S11 and Table S6, ESI†). Fig. 4(d) illustrates that the required overpotentials of the EE.300s HEA film were only 73 and 175 mV at current densities of 10 and 100 mA cm^{-2} under the neutral condition, and these values are much better than or close to those of the Pt sheet and commercial Pt/C nanoparticles and other reported values (Fig. S12 and Table S7, ESI†). Fig. S13 (ESI†) presents the corresponding Tafel slopes and Nyquist plots of the various HEA samples, indicating the fast reaction kinetics of EE.300s HEA film under both acidic and neutral conditions. These findings substantiate the hypothesis that the robust strain field effectively enhances the electrocatalytic activity.

Moreover, the mass activity of the EE.300s HEA film and Pt/C nanoparticles were gauged by standardizing the current

This journal is © The Royal Society of Chemistry 2024

Energy Environ. Sci., 2024, **17**, 5854–5865 | **5859**

Fig. 4 Electrochemical performances in 1.0 M KOH, 0.5 M H₂SO₄, and 1.0 M PBS solutions. (a) HER polarization curves and (b) Tafel plots of the HEA films in 1.0 M KOH solution. HER polarization curves in (c) 0.5 M H₂SO₄ and (d) 1.0 M PBS solutions. (e) and (f) Mass activities of the EE.300s film and Pt/C in 1.0 M KOH at various potentials. (g) Comparison of HER activities with recently reported noble-metal-based electrocatalysts in 1.0 M KOH at various current densities. (h) Faradaic efficiencies of EE.300s HEA film at various currents. (i) Schematic diagram of EE.300s‖IrO₂ AEM electrolyzer. (j) AEM performance using our EE.300s HEA film as the cathodic HER catalyst and commercial IrO₂ as the anodic OER catalyst at room temperature, insets show the photograph of the AEM water electrolyzer (right) and the performance of Pt/C‖IrO₂ AEM electrolyzer (left) for comparison.

density against the weight of the catalysts. As shown in Fig. 4(e) and (f), the EE.300s HEA film exhibited a considerably higher mass activity of 71.19 mA mg⁻¹ at an overpotential of 0.05 V (*vs.* RHE), approximately 11 times that of the Pt/C nanoparticles (6.45 mA mg⁻¹). We further evaluated the intrinsic catalytic activity by calculating the double-layer capacitances (C_{dl}) and turnover frequencies (TOFs) of the HEA films. C_{dl}, derived from the cyclic voltammogram curve (CV), disclosed that the EE.300s HEA film possesses the highest electrochemical active surface area (ECSA) (Fig. S14, ESI†), signifying the largest number of active sites on the surface of the various evaluated HEA films. Furthermore, the EE.300s HEA film achieved a TOF value of 0.254 s⁻¹ at an overpotential of 100 mV, substantially outperforming the as-dep,

EE.150s, and EE.800s HEA films with TOF values of 0.015, 0.178, and 0.19 s⁻¹, respectively, indicating that the vacancy-induced microstrain is able to effectively activate atomic sites and significantly improve the intrinsic activity of the HEA films. *In situ* Raman analysis offers further validation of the accelerated HER kinetics of the EE.300s HEA film (Fig. S15 and S16, ESI†). The peak located at 3432 cm⁻¹ was assigned to the characteristic peak of the interfacial H₂O molecules on the surface,[74,75] which gradually faded as the potential increased from open circuit potential to −11 mV for the as-dep HEA film, indicating the dissociation of the adsorbed H₂O molecules to intermediate species.[75–77] In particular, for the EE.300s HEA film, this peak vanished entirely at mere −8 mV, which is attributable to the rapid dissociation of H₂O molecules, as

5860 | *Energy Environ. Sci.*, 2024, **17**, 5854–5865

This journal is © The Royal Society of Chemistry 2024

supported by subsequent simulation results. We also evaluated the faradaic efficiency of the EE.300s HEA film at various currents. Videos S2–S6 (ESI†) show the measurement processes of the FE at various currents using a drainage method. As depicted in Fig. 4(h), the EE.300s HEA film consistently demonstrated faradaic efficiencies exceeding 96% at currents of 25, 50, 100, 200, and 500 mA.

The EE.300s HEA film also presented long lasting stability in a three-electrode system under universal pH conditions. The overpotential was not appreciably amplified during a ~ 60 h alkaline stability test at current densities of 10 and 100 mA cm^{-2} with negligible elemental leaching (Fig. S17 and Table S8, ESI†). In comparison, the performance of the Pt/C nanoparticles deteriorated by almost 300 mV after only 10 h of use at a current density of 100 mA cm^{-2}. We further evaluated their durability under acidic and neutral conditions, finding negligible degradation after working for one day (Fig. S18, ESI†). Furthermore, the structural and compositional stability of the EE.300s HEA film was also investigated after durability testing. It was found that the particulate-like surface morphology and the FCC structure of the used EE.300s HEA film were well maintained (Fig. S19a–c, ESI†). In terms of the elemental distributions, the relative content of Pt increased in the durability testing, while the contents of other elements decreased because of inevitable dissolution on the surface (Fig. S19d–j and Table S9, ESI†). The SAED pattern of the used EE.300s HEA film still exhibits the nanocrystalline characteristic with a *d*-spacing of 0.215 nm for the {111} plane (Fig. S20b and c, ESI†). A high concentration of vacancies on the used EE.300s HEA film surface was well retained (Fig. S20c1, ESI†). Moreover, obvious lattice distortion was observed in the used EE.300s HEA film, which was attributed to the microstrain aggregation during the process of vacancy generation and annihilation (Fig. S20c2, ESI†). XPS profiles of the used HEA film indicated that the zero-valent Fe, Co, Ni, and Cr elements transformed to higher valence states (Fig. S9, ESI†), suggesting a synergetic effect on the electrocatalysis performance of our multi-principal element alloy film. To test the sustainability of EE.300s HEA film for larger-scale hydrogen production, a flow-type AEM electrolyzer was assembled using EE.300s film as the cathode and IrO$_2$ as the anode (Fig. 4(i)). Significantly, the EE.300s||IrO$_2$ AEM electrolyzer enabled a current density of 100 mA cm^{-2} at a cell voltage of 2.0 V, with there being a minor deterioration of approximately 0.3 V after a duration of 20 days. In contrast, the power consumption of the reference Pt/C||IrO$_2$ system increased substantially, reaching 150% of its initial value after only 13 hours (Fig. 4(j)).

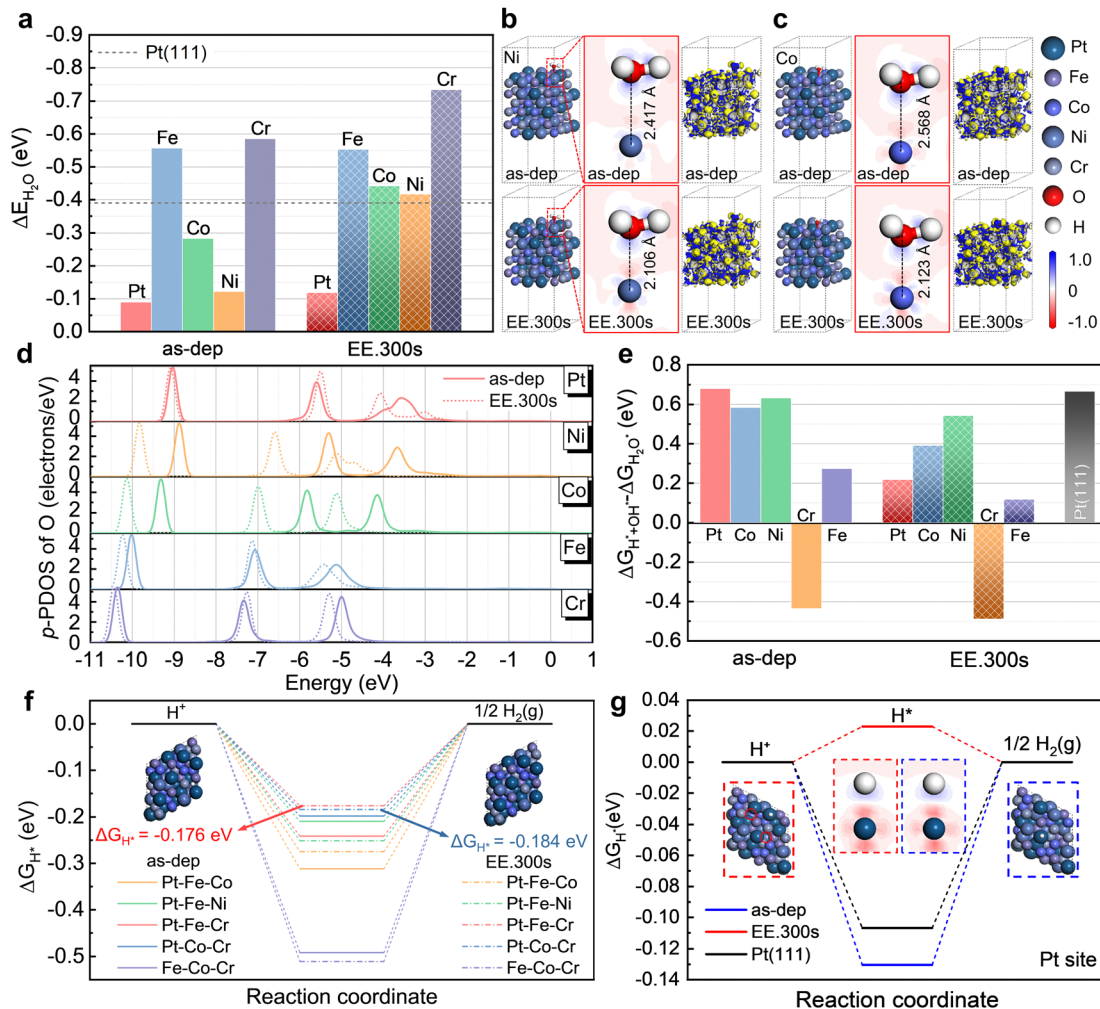### Density functional theory (DFT) calculations

First-principle calculations were conducted to elucidate the atomistic mechanism driving the HER process in the context of the FeCoNiCrPt HEA films by contrasting the as-dep and EE.300s models. The adsorption energy of H$_2$O ($\Delta E_{\text{H}_2\text{O}}$) emerged as a crucial factor affecting the HER performance of the electrocatalysts. Consequently, $\Delta E_{\text{H}_2\text{O}}$ values at various active sites for the as-dep and EE.300s models were calculated as presented in Fig. 5(a). Notably, it was found that the H$_2$O molecules displayed a preference for stabilization at single-atom top sites with distinct

$\Delta E_{\text{H}_2\text{O}}$ values. In the as-dep model, Fe and Cr sites exhibited H$_2$O adsorption capacities superior to that of Pt (111), suggesting their potential roles in enhancing H$_2$O adsorption efficiency. Intriguingly, the H$_2$O adsorption capacities at all the Fe, Co, Ni, and Cr sites in the EE.300s model outperform that of the Pt (111), with the Cr site having the strongest adsorption capacity. These results indicate that the vacancy-induced microstrain in the EE.300s film significantly enhanced the H$_2$O adsorption performance across all active sites, which would be an important contribution to the H$_2$O molecule dissociation step. Active sites and their corresponding electron density differences following H$_2$O adsorption at Co, Ni, and other sites of the as-dep and EE.300s models are depicted in Fig. 5(b), (c) and Fig. S21, S22 (ESI†). These results reveal divergent electron density differences between the active sites, indicative of distinct charge transfer capabilities potentially due to different atomic strain statuses.

The implications of the differences in $\Delta E_{\text{H}_2\text{O}}$ were explored by comparing active sites between the two models (Table S10, ESI†). All bonding distances between the O atom in H$_2$O and Fe/Co/Ni/Cr/Pt sites in the EE.300s model were shorter than the corresponding ones in the as-dep model, particularly at Co/Ni/Cr sites, yielding substantial improvements in $\Delta E_{\text{H}_2\text{O}}$. Accordingly, the enhanced $\Delta E_{\text{H}_2\text{O}}$ at the active sites in the EE.300s model can be explained by their stronger interactions relative to those of identical element sites in the as-dep counterpart, leading to reduced bonding distances. Variations in charge transfer capabilities for Ni (Fig. 5(b)), Co (Fig. 5(c)), and Cr (Fig. S23, ESI†) sites between the as-dep and EE.300s models were also evident from local two-dimensional (2D) electron density differences, suggesting that charge transfer from the active sites to H$_2$O molecules can be augmented in the EE.300s model. Therefore, the electrochemical etching process effectively enhanced the H$_2$O adsorption capacity of the FeCoNiCrPt HEA film and this enhancement was primarily owing to increased interaction between H$_2$O molecules and Co, Ni, and Cr sites, under the influence of vacancies and microstrain.

The binding strength between H$_2$O molecules and active sites was further explored through analyzing the partial density of states (PDOS), as depicted in Fig. S24 and S25 (ESI†). The adsorbed O atom in H$_2$O molecules exhibited a clear affinity for all of the active sites. However, there were distinct hybridization energy levels for the as-dep and EE.300s models. The sequence of H$_2$O adsorption ability increased in the order of Pt < Ni < Co < Fe < Cr, with a notable left shift of the hybridization energy positions away from the Fermi level as the H$_2$O adsorption ability increased, signifying an element-dependent H$_2$O adsorption ability for FeCoNiCrPt HEA.[78] Furthermore, a similar significant left shift of the interaction positions away from the Fermi level was observed for all active sites in the EE.300s model similar to that seen in the as-dep model (Fig. 5(d)).

The H$_2$O molecule dissociation step, another pivotal factor affecting the HER performance, was also investigated for the as-dep and EE.300s models (Fig. 5(e) and Fig. S26, ESI†). Previous reports suggested that the H$_2$O dissociation step has a thermodynamical upslope on Pt (111),[79] whereas a thermodynamical downslope is typically preferred for efficient HER performance.

This journal is © The Royal Society of Chemistry 2024

Energy Environ. Sci., 2024, **17**, 5854–5865 | **5861**

Fig. 5 DFT simulation results. (a) Adsorption energy of H_2O molecules on Pt, Fe, Co, Ni, and Cr sites of the as-dep and EE.300s models. As a reference, the adsorption energy of H_2O molecules on the Pt (111) surface is marked by the grey dashed line. Atomic configurations and electron density difference of the as-dep and EE.300s models after H_2O adsorption onto (b) Ni and (c) Co sites, respectively. Yellow and blue isosurfaces represent the depletion and segregation of electrons, respectively. (d) p-PDOS of the O atoms in an H_2O molecule after H_2O adsorption onto Pt, Ni, Co, Fe, and Cr sites in the as-dep and EE.300s models. (e) Corresponding energy change during the dissociation of H_2O^* to H^* and OH^*. Gibbs free energy (ΔG_{H^*}) profiles on (f) triple-atom sites and (g) Pt sites at the surfaces of the as-dep and EE.300s models. The insets in (f) are the corresponding atomic configurations after H^* adsorption onto Pt–Fe–Cr and Pt–Co–Cr sites of EE.300s models. The insets in (g) are the corresponding atomic configurations after H^* adsorption onto Pt sites of the as-dep and EE.300s models with vacancies highlighted by red circles.

As shown in Fig. 5(e), the Cr site had a thermodynamical downslope for both the as-dep and EE.300s models, indicating the crucial role of the Cr element in optimizing the H_2O dissociation step. Moreover, the barrier for H_2O dissociation at all active sites was effectively reduced by the etching process, indicating the potential for enhanced H_2O dissociation rates at active sites in the EE.300s model. The enhancement accelerated the supply of hydrogen protons (H^*), thereby promoting the HER process.

The Gibbs free energy of H^* (ΔG_{H^*}) is a recognized descriptor of the HER performance, with values approaching zero deemed advantageous for the reversible adsorption and desorption of H^*.[80,81] We undertook the DFT calculation-based analysis of ΔG_{H^*}, yielding a range of values following H^* adsorption at diverse sites of the as-dep and EE.300s models (Table S11, ESI†).

The stable triple-atom sites are documented in Fig. S27 and S28 (ESI†). Fig. 5(f) reveals significant improvements in ΔG_{H^*} value towards zero at Pt–Fe–Co, Pt–Fe–Cr, and Pt–Co–Cr sites within the microstrained EE.300s model. Furthermore, H^* achieved stability at single-atom Pt sites with a ΔG_{H^*} close to zero (Fig. 5(g)). More importantly, ΔG_{H^*} values of the Pt sites in the as-dep and EE.300s models were inferior and superior to those of Pt (111), respectively, indicating the critical role of strain engineering in enhancing the HER performance.

Given that the Pt sites in the EE.300s model display the most favorable ΔG_{H^*} values for exceptional HER performance, our primary focus was deciphering the physical mechanism and contrasting it with that of the as-dep model. The electron transfer ability between H^* and Pt sites were analyzed by examining the 2D electron density difference after H^* adsorption onto Pt sites in

5862 | *Energy Environ. Sci.*, 2024, **17**, 5854–5865

This journal is © The Royal Society of Chemistry 2024

both the as-dep and EE.300s models (Fig. S29, ESI†). An analysis of the 2D electron density difference revealed that the electron transfer propensity of Pt sites in the EE.300s model was less than that in the as-dep model. Moreover, the d-band centers for the Pt sites in the EE.300s model significant shifted farther from the Fermi level (Fig. S30, ESI†), suggesting that the vacancy-induced microstrain in crystalline lattice weakens the overly strong interaction strength between H* and Pt sites, thus optimizing ΔG_{H*}.

Conclusions

In summary, we employed an innovative strain-engineering approach to create a microstrained FeCoNiCrPt HEA film. This microstrained HEA film demonstrates superior HER performance under pH-universal conditions, along with exceptional sustainability. We ascribe this enhanced electrocatalytic activity to the strain-induced optimization of charge distribution. The prevailing tensile strain surrounding the Pt atoms and the compressive strain around vacancies modulate the Pt–Pt and Pt–M (M = Fe, Co, Ni, Cr) bond lengths, as well as the positioning of the d-band center. This leads to a decrease in the binding energy of intermediates and the HER barrier while maintaining stellar catalyst durability. The newly developed FeCoNiCrPt HEA film exhibits exceptional capabilities for industrial water electrolysis, achieving an ampere-level current density of 1 A cm^{-2} with overpotentials of 104 and 106 mV in alkaline and acidic conditions, respectively. Furthermore, it displays impressive sustainability, maintaining ~500 h at 100 mA cm^{-2} using an AEM electrolyzer, which equates to a lifespan 40 times longer than the commercial Pt/C||IrO$_2$ system. This research not only provides evidence of a robust and highly efficient HER catalyst that can enhance industrial hydrogen production, but it also sheds light on the significant role of lattice strain in electrocatalysis. These findings pave the way for the design and development of future catalysts for sustainable energy conversion.

Author contributions

Conceptualization: Z. J. and B. L. S., methodology: Y. Y. Y., Q. Q. W., Y. J. L., L. G. S., B. S., J. K., S. D., J. H., S. L., L. D., and H. T., investigation: Y. Y. Y., Q. Q. W., Y. J. L., L. G. S., B. S., J. K., S. D., J. H., S. L., L. D., and H. T., visualization: Y. Y. Y., Z. J., L. G. S., Y. J. L., funding acquisition: Z. J., L. G. S., and B. L. S., project administration: Z. J., L. G. S., and B. L. S., supervision: Z. J., L. G. S., and B. L. S., writing – original draft: Y. Y. Y., Z. J., and L. G. S., writing – review & editing: Y. Y. Y., Z. J., L. G. S., Q. Q. W., L. C. Z., J. J. K., J. L., and B. L. S.

Conflicts of interest

There are no conflicts to declare.

Acknowledgements

References

1 D. A. Cullen, K. C. Neyerlin, R. K. Ahluwalia, R. Mukundan, K. L. More, R. L. Borup, A. Z. Weber, D. J. Myers and A. Kusoglu, *Nat. Energy*, 2021, **6**, 462–474.

2 B. C. H. Steele and A. Heinze, *Nature*, 2001, **414**, 345–352.

3 M. F. Lagadec and A. Grimaud, *Nat. Mater.*, 2020, **19**, 1140–1150.

4 Z.-J. Zhao, S. Liu, S. Zha, D. Cheng, F. Studt, G. Henkelman and J. Gong, *Nat. Rev. Mater.*, 2019, **4**, 792–804.

5 H. Sun, X. Xu, H. Kim, W. Jung, W. Zhou and Z. Shao, *Energy Environ. Mater.*, 2023, e12441.

6 S.-P. Zeng, H. Shi, T.-Y. Dai, Y. Liu, Z. Wen, G.-F. Han, T.-H. Wang, W. Zhang, X.-Y. Lang, W.-T. Zheng and Q. Jiang, *Nat. Commun.*, 2023, **14**, 1811.

7 Y. Chen, S. Ji, C. Chen, Q. Peng, D. Wang and Y. Li, *Joule*, 2018, **2**, 1242–1264.

8 X. Lei, Q. Tang, Y. Zheng, P. Kidkhunthod, X. Zhou, B. Ji and Y. Tang, *Nat. Sustain.*, 2023, **6**, 816–826.

9 L. Peng, N. Yang, Y. Yang, Q. Wang, X. Xie, D. Sun-Waterhouse, L. Shang, T. Zhang and G. I. N. Waterhouse, *Angew. Chem., Int. Ed.*, 2021, **60**, 24612–24619.

10 D. Wang, Q. Li, C. Han, Q. Lu, Z. Xing and X. Yang, *Nat. Commun.*, 2019, **10**, 3899.

11 J. Zhang, Y. Zhao, X. Guo, C. Chen, C.-L. Dong, R.-S. Liu, C.-P. Han, Y. Li, Y. Gogotsi and G. Wang, *Nat. Catal.*, 2018, **1**, 985–992.

12 S. Zhu, X. Qin, F. Xiao, S. Yang, Y. Xu, Z. Tan, J. Li, J. Yan, Q. Chen, M. Chen and M. Shao, *Nat. Catal.*, 2021, **4**, 711–718.

13 X. Zhang, P. Yu, X. Su, S. Hu, L. Shi, Y. Wang, P. Yang, F. Gao, Z. Wu, L. Chi, Y. Zheng and M. Gao, *Sci. Adv.*, 2023, **9**, eadh2885.

14 X. Lu, L. Yu and X. Lou, *Sci. Adv.*, 2019, **5**, eaav6009.

15 L. Li, B. Wang, G. Zhang, G. Yang, T. Yang, S. Yang and S. Yang, *Adv. Energy Mater.*, 2020, **10**, 2001600.

16 Y. Li, Z. G. Yu, L. Wang, Y. Weng, C. S. Tang, X. Yin, K. Han, H. Wu, X. Yu, L. M. Wong, D. Wan, X. R. Wang, J. Chai, Y.-W. Zhang, S. Wang, J. Wang, A. T. S. Wee, M. B. H. Breese, S. J. Pennycook, T. Venkatesan, S. Dong, J. M. Xue and J. Chen, *Nat. Commun.*, 2019, **10**, 3140.

17 Y. Yao, Q. Dong, A. Brozena, J. Luo, J. Miao, M. Chi, C. Wang, I. G. Kevrekidis, Z. J. Ren, J. Greeley, G. Wang, A. Anapolsky and L. Hu, *Science*, 2022, **376**, eabn3103.

18 Y. Sun and S. Dai, *Sci. Adv.*, 2021, 7, eabg1600.

19 Y. Ma, Y. Ma, Q. Wang, S. Schweidler, M. Botros, T. Fu, H. Hahn, T. Brezesinski and B. Breitung, *Energy Environ. Sci.*, 2021, **14**, 2883–2905.

This journal is © The Royal Society of Chemistry 2024

Energy Environ. Sci., 2024, **17**, 5854–5865 | **5863**

20 X. Zeng, Y. Jing, S. Gao, W. Zhang, Y. Zhang, H. Liu, C. Liang, C. Ji, Y. Rao, J. Wu, B. Wang, Y. Yao and S. Yang, *Nat. Commun.*, 2023, **14**, 7414.

21 H. Shi, X. Y. Sun, Y. Liu, S. P. Zeng, Q. H. Zhang, L. Gu, T. H. Wang, G. F. Han, Z. Wen, Q. R. Fang, X. Y. Lang and Q. Jiang, *Adv. Funct. Mater.*, 2023, **33**, 2214412.

22 Z. Jia, T. Yang, L. Sun, Y. Zhao, W. Li, J. Luan, F. Lyu, L. C. Zhang, J. J. Kruzic, J. J. Kai, J. C. Huang, J. Lu and C. T. Liu, *Adv. Mater.*, 2020, **32**, 2000385.

23 Y. Yang, Z. Jia, X. Zhang, Y. Liu, Q. Wang, Y. Li, L. Shao, S. Di, J. Kuang, L. Sun, L.-C. Zhang, J. J. Kruzic, Y. Lu, J. Lu and B. Shen, *Mater. Today*, 2024, **72**, 112–123.

24 H. Zhu, S. Sun, J. Hao, Z. Zhuang, S. Zhang, T. Wang, Q. Kang, S. Lu, X. Wang, F. Lai, T. Liu, G. Gao, M. Du and D. Wang, *Energy Environ. Sci.*, 2023, **16**, 619–628.

25 Z. W. Chen, J. Li, P. Ou, J. E. Huang, Z. Wen, L. Chen, X. Yao, G. Cai, C. C. Yang, C. V. Singh and Q. Jiang, *Nat. Commun.*, 2024, **15**, 359.

26 T. Li, Y. Yao, Z. Huang, P. Xie, Z. Liu, M. Yang, J. Gao, K. Zeng, A. H. Brozena, G. Pastel, M. Jiao, Q. Dong, J. Dai, S. Li, H. Zong, M. Chi, J. Luo, Y. Mo, G. Wang, C. Wang, R. Shahbazian-Yassar and L. Hu, *Nat. Catal.*, 2021, **4**, 62–70.

27 M. Cui, C. Yang, B. Li, Q. Dong, M. Wu, S. Hwang, H. Xie, X. Wang, G. Wang and L. Hu, *Adv. Energy Mater.*, 2020, **11**, 2002887.

28 M. Cui, C. Yang, S. Hwang, M. Yang, S. Overa, Q. Dong, Y. Yao, A. H. Brozena, D. A. Cullen, M. Chi, T. F. Blum, D. Morris, Z. Finfrock, X. Wang, P. Zhang, V. G. Goncharov, X. Guo, J. Luo, Y. Mo, F. Jiao and L. Hu, *Sci. Adv.*, 2022, **8**, eabm4322.

29 Z. Jia, K. Nomoto, Q. Wang, C. Kong, L. Sun, L. C. Zhang, S. X. Liang, J. Lu and J. J. Kruzic, *Adv. Funct. Mater.*, 2021, **31**, 2101586.

30 X. Zhang, Y. Yang, Y. Liu, Z. Jia, Q. Wang, L. Sun, L. C. Zhang, J. J. Kruzic, J. Lu and B. Shen, *Adv. Mater.*, 2023, **35**, 2303439.

31 S. C. Kim, J. Wang, R. Xu, P. Zhang, Y. Chen, Z. Huang, Y. Yang, Z. Yu, S. T. Oyakhire, W. Zhang, L. C. Greenburg, M. S. Kim, D. T. Boyle, P. Sayavong, Y. Ye, J. Qin, Z. Bao and Y. Cui, *Nat. Energy*, 2023, **8**, 814–826.

32 C. Yang, J. Xia, C. Cui, T. P. Pollard, J. Vatamanu, A. Faraone, J. A. Dura, M. Tyagi, A. Kattan, E. Thimsen, J. Xu, W. Song, E. Hu, X. Ji, S. Hou, X. Zhang, M. S. Ding, S. Hwang, D. Su, Y. Ren, X.-Q. Yang, H. Wang, O. Borodin and C. Wang, *Nat. Sustain.*, 2023, **6**, 325–335.

33 J.-W. Yeh, *Ann. Chim-Sci. Mat.*, 2006, **31**, 633–648.

34 B. Cantor, *Entropy*, 2014, **16**, 4749–4768.

35 M.-H. Tsai and J.-W. Yeh, *Mater. Res. Lett.*, 2014, **2**, 107–123.

36 M. Wei, Y. Sun, J. Zhang, F. Ai, S. Xi and J. Wang, *Energy Environ. Sci.*, 2023, **16**, 4009–4019.

37 H. Wang, S. Xu, C. Tsai, Y. Li, C. Liu, J. Zhao, Y. Liu, H. Yuan, F. Abild-Pedersen, F. B. Prinz, J. K. Nørskov and Y. Cui, *Science*, 2016, **354**, 1031–1036.

38 Z. Xia and S. Guo, *Chem. Soc. Rev.*, 2019, **48**, 3265–3278.

39 G. Liu, A. J. Shih, H. Deng, K. Ojha, X. Chen, M. Luo, I. T. McCrum, M. T. M. Koper, J. Greeley and Z. Zeng, *Nature*, 2024, **626**, 1005–1010.

40 S. Maiti, K. Maiti, M. T. Curnan, K. Kim, K.-J. Noh and J. W. Han, *Energy Environ. Sci.*, 2021, **14**, 3717–3756.

41 H. Liang, W. Yang, J. Xia, H. Gu, X. Meng, G. Yang, Y. Fu, B. Wang, H. Cai, Y. Chen, S. Yang and C. Liang, *Adv. Sci.*, 2023, **10**, e2304733.

42 R. Chattot, O. Le Bacq, V. Beermann, S. Kuhl, J. Herranz, S. Henning, L. Kuhn, T. Asset, L. Guetaz, G. Renou, J. Drnec, P. Bordet, A. Pasturel, A. Eychmuller, T. J. Schmidt, P. Strasser, L. Dubau and F. Maillard, *Nat. Mater.*, 2018, **17**, 827–833.

43 D. Wang, Z. Chen, Y.-C. Huang, W. Li, J. Wang, Z. Lu, K. Gu, T. Wang, Y. Wu, C. Chen, Y. Zhang, X. Huang, L. Tao, C.-L. Dong, J. Chen, C. V. Singh and S. Wang, *Sci. China Mater.*, 2021, **64**, 2454–2466.

44 T. He, W. Wang, F. Shi, X. Yang, X. Li, J. Wu, Y. Yin and M. Jin, *Nature*, 2021, **598**, 76–81.

45 M. Li, Z. Zhao, Z. Xia, M. Luo, Q. Zhang, Y. Qin, L. Tao, K. Yin, Y. Chao, L. Gu, W. Yang, Y. Yu, G. Lu and S. Guo, *Angew. Chem., Int. Ed.*, 2021, **60**, 8243–8250.

46 K. Jiang, M. Luo, Z. Liu, M. Peng, D. Chen, Y. R. Lu, T. S. Chan, F. M. F. de Groot and Y. Tan, *Nat. Commun.*, 2021, **12**, 1687.

47 Y. Shi, Z. Lyu, M. Zhao, R. Chen, Q. N. Nguyen and Y. Xia, *Chem. Rev.*, 2021, **121**, 649–735.

48 S. Hao, H. Sheng, M. Liu, J. Huang, G. Zheng, F. Zhang, X. Liu, Z. Su, J. Hu, Y. Qian, L. Zhou, Y. He, B. Song, L. Lei, X. Zhang and S. Jin, *Nat. Nanotechnol.*, 2021, **16**, 1371–1377.

49 R. Chattot, T. Asset, P. Bordet, J. Drnec, L. Dubau and F. Maillard, *ACS Catal.*, 2016, **7**, 398–408.

50 R. G. Mariano, K. McKelvey, H. S. White and M. W. Kanan, *Science*, 2017, **358**, 1187–1192.

51 A. Khorshidi, J. Violet, J. Hashemi and A. A. Peterson, *Nat. Catal.*, 2018, **1**, 263–268.

52 Y. He, Q. Shi, W. Shan, X. Li, A. J. Kropf, E. C. Wegener, J. Wright, S. Karakalos, D. Su, D. A. Cullen, G. Wang, D. J. Myers and G. Wu, *Angew. Chem., Int. Ed.*, 2021, **60**, 9516–9526.

53 B. You, M. T. Tang, C. Tsai, F. Abild-Pedersen, X. Zheng and H. Li, *Adv. Mater.*, 2019, **31**, e1807001.

54 H. Guo, L. Li, Y. Chen, W. Zhang, C. Shang, X. Cao, M. Li, Q. Zhang, H. Tan, Y. Nie, L. Gu and S. Guo, *Adv. Mater.*, 2023, **35**, e2302285.

55 L. Wang, Z. Zeng, W. Gao, T. Maxson, D. Raciti, M. Giroux, X. Pan, C. Wang and J. Greeley, *Science*, 2019, **363**, 870–874.

56 L. Dubau, J. Nelayah, T. Asset, R. Chattot and F. Maillard, *ACS Catal.*, 2017, **7**, 3072–3081.

57 Z. Li, Q. Wang, X. Bai, M. Wang, Z. Yang, Y. Du, G. E. Sterbinsky, D. Wu, Z. Yang, H. Tian, F. Pan, M. Gu, Y. Liu, Z. Feng and Y. Yang, *Energy Environ. Sci.*, 2021, **14**, 5035–5043.

58 Y. Sun, Y. Liang, M. Luo, F. Lv, Y. Qin, L. Wang, C. Xu, E. Fu and S. Guo, *Small*, 2018, **14**, 1702259.

59 C. Li, Q. Yuan, B. Ni, T. He, S. Zhang, Y. Long, L. Gu and X. Wang, *Nat. Commun.*, 2018, **9**, 3702.

60 F. Yang, A. O. Elnabawy, R. Schimmenti, P. Song, J. Wang, Z. Peng, S. Yao, R. Deng, S. Song, Y. Lin, M. Mavrikakis and W. Xu, *Nat. Commun.*, 2020, **11**, 1088.

61 J. Hao, Z. Zhuang, J. Hao, K. Cao, Y. Hu, W. Wu, S. Lu, C. Wang, N. Zhang, D. Wang, M. Du and H. Zhu, *ACS Nano*, 2022, **16**, 3251–3263.

5864 | *Energy Environ. Sci.*, 2024, **17**, 5854–5865

This journal is © The Royal Society of Chemistry 2024

62 X. Tian, X. Zhao, Y.-Q. Su, L. Wang, H. Wang, D. Dang, B. Chi, H. Liu, E. J. M. Hensen, X. W. D. Lou and B. Y. Xia, *Science*, 2019, **366**, 850–856.

63 J. Baek, M. D. Hossain, P. Mukherjee, J. Lee, K. T. Winther, J. Leem, Y. Jiang, W. C. Chueh, M. Bajdich and X. Zheng, *Nat. Commun.*, 2023, **14**, 5936.

64 J. Gu, L. Li, Y. Xie, B. Chen, F. Tian, Y. Wang, J. Zhong, J. Shen and J. Lu, *Nat. Commun.*, 2023, **14**, 5389.

65 Y. Chida, T. Tomimori, T. Ebata, N. Taguchi, T. Ioroi, K. Hayashi, N. Todoroki and T. Wadayama, *Nat. Commun.*, 2023, **14**, 4492.

66 S. Dai, J. Yu, J. He, Y. Liu, Z. Mo, E. Wu and J. Meng, *Appl. Phys. Express*, 2021, **14**, 075501.

67 C. W. Zhao, Y. M. Xing, C. E. Zhou and P. C. Bai, *Acta Mater.*, 2008, **56**, 2570–2575.

68 Y. Wu, J. Wang, Y. He, H. Wu, C. Jiang and H. Xu, *Acta Mater.*, 2016, **104**, 91–100.

69 X. Sun, D. Wu, L. Zou, S. D. House, X. Chen, M. Li, D. N. Zakharov, J. C. Yang and G. Zhou, *Nature*, 2022, **607**, 708–713.

70 C. Sun, T. Paulauskas, F. G. Sen, G. Lian, J. Wang, C. Buurma, M. K. Chan, R. F. Klie and M. J. Kim, *Sci. Rep.*, 2016, **6**, 27009.

71 D. B. Miracle and O. N. Senkov, *Acta Mater.*, 2017, **122**, 448–511.

72 Y. Zhao, Y. Zhao, R. Shi, B. Wang, G. I. N. Waterhouse, L. Z. Wu, C. H. Tung and T. Zhang, *Adv. Mater.*, 2019, **31**, 1806482.

73 Y. Sun, S. Gao, F. Lei and Y. Xie, *Chem. Soc. Rev.*, 2015, **44**, 623–636.

74 K. Kamali and C. Narayana, *Mater. Today: Proc.*, 2022, **49**, 1196–1199.

75 X. Chen, X. T. Wang, J. B. Le, S. M. Li, X. Wang, Y. J. Zhang, P. Radjenovic, Y. Zhao, Y. H. Wang, X. M. Lin, J. C. Dong and J. F. Li, *Nat. Commun.*, 2023, **14**, 5289.

76 H. Tan, B. Tang, Y. Lu, Q. Ji, L. Lv, H. Duan, N. Li, Y. Wang, S. Feng, Z. Li, C. Wang, F. Hu, Z. Sun and W. Yan, *Nat. Commun.*, 2022, **13**, 2024.

77 J. Duan, T. Liu, Y. Zhao, R. Yang, Y. Zhao, W. Wang, Y. Liu, H. Li, Y. Li and T. Zhai, *Nat. Commun.*, 2022, **13**, 2039.

78 Z. Chen, Y. Xu, D. Ding, G. Song, X. Gan, H. Li, W. Wei, J. Chen, Z. Li, Z. Gong, X. Dong, C. Zhu, N. Yang, J. Ma, R. Gao, D. Luo, S. Cong, L. Wang, Z. Zhao and Y. Cui, *Nat. Commun.*, 2022, **13**, 763.

79 F. Li, G. F. Han, H. J. Noh, Y. Lu, J. Xu, Y. Bu, Z. Fu and J. B. Baek, *Angew. Chem., Int. Ed.*, 2018, **57**, 14139–14143.

80 J. Greeley, T. F. Jaramillo, J. Bonde, I. B. Chorkendorff and J. K. Norskov, *Nat. Mater.*, 2006, **5**, 909–913.

81 J. K. Nørskov, T. Bligaard, A. Logadottir, J. R. Kitchin, J. G. Chen, S. Pandelov and U. Stimming, *J. Electrochem. Soc.*, 2005, **152**, J23–J26.

This journal is © The Royal Society of Chemistry 2024

Energy Environ. Sci., 2024, **17**, 5854–5865 | **5865**